Surface extended x-ray absorption fine structure studies of metastable magnetic thin films and nanostructures

2003 J. Phys.: Condens. Matter 15 S657

(http://iopscience.iop.org/0953-8984/15/5/319)

INSTITUTE OF PHYSICS PUBLISHING JOURNAL OF PHYSICS: CONDENSED MATTER

J. Phys.: Condens. Matter **15** (2003) S657–S678 PII: S0953-8984(03)54553-2

Surface extended x-ray absorption fine structure studies of metastable magnetic thin films and nanostructures

D Chandesris[1], P Le Fèvre[1], H Magnan[1,2], A Chaumin-Midoir[1,3], H Jaffrès[4,6], F Scheurer[5] and L Barbier[2]

[1] Laboratoire pour l'Utilisation du Rayonnement Electromagnétique, CNRS-CEA-Université Paris Sud, BP 34, 91898 Orsay Cedex, France
[2] Service de Physique et Chimie des Surfaces et Interfaces, DSM/DRECAM, CEA/Saclay, 91191 Gif-sur-Yvette Cedex, France
[3] Groupe de Physique des Matériaux Denses, Université Paris XII, 61 Avenue du général de Gaulle, 94010 Créteil Cedex, France
[4] Laboratoire de Physique de la Matière Condensée, CNRS-Université Paul Sabattier-INSA, 31077 Toulouse Cedex, France
[5] Institut de Physique et Chimie des Matériaux de Strasbourg, CNRS-Université Louis Pasteur, 23 rue du Loess, 67037 Strasbourg, France

Received 9 October 2002
Published 27 January 2003
Online at stacks.iop.org/JPhysCM/15/S657

Abstract

Magnetic films deposited on single-crystal substrates have been the subject of numerous studies since their bi-dimensional or nanostructured character provides important extensions of the family of bulk magnetic solids. For these objects, the knowledge of their size, shape and structure at the atomic scale are mandatory for an understanding of their unusual magnetic properties. After a short introduction to the strengths of extended x-ray absorption fine structure (EXAFS) for local structure determination, we will concentrate on three well defined cases. Thin Ni layers deposited on Cu(001) present a perpendicular magnetic anisotropy in a very wide thickness range, and thin Fe layers on MgO(001) cut into stripes by the 'atomic saw' (AS) method have a magnetization easy axis oriented perpendicular to the stripes. In both cases, a precise structural characterization obtained by EXAFS and simple magneto-elastic models allow description of their magnetic behaviour. The growth of a cobalt film on a vicinal Cu(11n) surface induces a uniaxial magnetic anisotropy. Although the steps are clearly at the origin of this behaviour, the exact mechanism (lower coordination at step edges, anisotropic strain) remains obscure. Detailed studies of the morphology by STM and of the structure by EXAFS allow the conclusion that the step-induced magnetic anisotropy does not originate from an in-plane anisotropic structural relaxation but is more likely related to the stepped film morphology.

[6] Present address: Unité Mixte de Physique CNRS/THALES, Domaine de Corbeville, 91404 Orsay, France.

1. Introduction

Thin films deposited on single-crystal substrates have been the subjects of numerous studies during the last decade. It appeared that one could stabilize original crystallographic phases for a large range of elements, thus creating a new class of materials. Their bi-dimensional character, together with the occurrence of singular crystallographic structures, often confer to these thin films electronic properties that cannot be found in bulk solids. Moreover, these systems provide new opportunities to explore the relationship between structure and magnetism. The magnetic properties of 3d transition metal thin films are governed by magnetic anisotropies, which were found to be several orders of magnitude larger than in bulk materials. Since the observation of perpendicular magnetic anisotropy (PMA) in ultra-thin magnetic films, the influence of symmetry breaking at interfaces and the influence of epitaxial strains on magnetic anisotropy has been widely discussed [1–5]. Magnetic anisotropy in thin films arises both from dipole–dipole and spin–orbit interaction. Spin–orbit interaction, which couples magnetization orientation and crystallographic structure, is at the origin of magneto-crystalline anisotropy (symmetry of the lattice), magneto-elastic effects (local strain) and Néel type surface anisotropy (missing bonds at the surface).

In this paper, we present three structural studies of magnetic ultra-thin films and nanostructures using extended x-ray absorption fine structure (EXAFS). We will show that a precise crystallographic characterization of these systems is of key importance for understanding their magnetic behaviour via simple magneto-elastic models. The paper is organized as follows: in the second section, in order to establish the potentiality of EXAFS for structural characterization of metastable thin films, we present results on reference crystals of different structures and show how precisely the experimental data and their polarization dependence can be reproduced by theoretical simulations. The structure study of thin Ni films on Cu(001) will be presented in section 3. The results validate the magnetic models proposed to explain the PMA in this system. Section 4 will deal with Fe layers deposited on MgO(001), patterned into ribbons by the AS method. In these nanostructures, Fe exhibits a magnetization easy axis surprisingly aligned perpendicular to the ribbons. The EXAFS study shows that the effect of the structuring process is mainly to relax the epitaxial strain perpendicular to the ribbon's edge, and a simple magneto-elastic model can once again account for the magnetic anisotropy. In section 5, a detailed study of the origin of the twofold anisotropy in Co/Cu($11n$) is performed. The growth of Co films on a stepped Cu($11n$) surface produces a step-induced uniaxial magnetic anisotropy which has been discussed as a magneto-elastic effect or within the Néel model considering the missing bonds at the step edge. However, the variation of magnetic anisotropy with film thickness and density of steps remains unexplained. We used the combination of two techniques, scanning tunnelling microscopy (STM) and surface EXAFS at the K edge of cobalt to determine both the morphology and crystallographic structure of the films. While the surface morphology undergoes strong evolutions upon cobalt growth (as seen by STM), EXAFS measurements give a quasi-constant and isotropic in-plane cobalt lattice parameter. So, in this case, the step-induced anisotropy is not due to in-plane magneto-elastic anisotropy but rather results from the morphology of the film. A model describing the magnetic anisotropy has to take into account the missing bonds at the step edges of islands and the presence of faceting.

The EXAFS experiments were performed at the Laboratoire pour l'Utilisation du Rayonnement Electromagnétique (LURE) on the surface EXAFS set-up using a Si(311) double-crystal monochromator installed on the wiggler beam line of the DCI storage ring. The incident beam is linearly polarized and the sample can be rotated in order to align the polarization direction with different symmetry axes. The samples are maintained at 77 K in order to reduce the thermal disorder and improve the precision of the crystallographic characterization.

2. Simulations of the EXAFS spectra and their anisotropies using the FEFF code

Surface extended x-ray absorption fine structure (SEXAFS) consists in measuring the absorption coefficient of the sample as a function of the incoming photon energy. The oscillations of the x-ray absorption coefficient (EXAFS oscillations) are due to perturbations to the absorption of an isolated atom by its surrounding neighbours. These oscillations are therefore directly correlated to the structure and the local order around the excited atom. A Fourier transform (FT) of the EXAFS oscillations gives a series of peaks corresponding to the different shells of neighbours of the excited atom [6]. An inverse Fourier transform (IFT) of the first peak of the FT allows isolation of the contribution of the first nearest neighbour (FNN) shell from the total signal. In the simple case where this nearest neighbour (NN) shell is constituted from atoms of the same atomic species, located at a unique distance R_1 from the excited atom, this contribution χ_1 can be fitted using a simple formula

$$\chi_1(k) = -\frac{N_1^*}{kR_1^2} B(k) \mathrm{e}^{-2k^2\sigma^2} \sin(2kR_1 + \varphi(k)). \tag{1}$$

χ_1 is given as a function of k, the wavevector of the photoelectron created in the absorption process, which is related to the photon energy $h\nu$ by

$$h\nu - E_l = \frac{\hbar^2 k^2}{2m}$$

where E_l is the binding energy of the core level. $B(k)$ (neighbouring atom backscattering amplitude) and $\varphi(k)$ (phase shift) are electronic parameters. They are often determined from EXAFS spectra of reference materials with a well established crystallographic structure. Knowing the electronic parameters, one can then extract the crystallographic parameters (R_1, σ^2 and N_1^*) by fitting the experimental data with formula (1). R_1 is the FNN distance, and σ^2 is the mean square relative displacement, giving the width of the radial distribution function. N_1^* is an apparent number of FNNs, which, in the case of the K edge, is given by the simple formula

$$N_1^* = 3 \sum_{j=1}^{N_1} \cos^2 \alpha_j \tag{2}$$

where α_j is the angle between the polarization of the x-rays and the bond between the absorbing atom and its jth FNN. From this formula, it appears that the EXAFS oscillations depend on the polarization direction of the x-rays with respect to the sample crystallographic structure: the contribution of each bond to the total signal is weighted by a the cosine of the square of the angle between the bond and the polarization of the light. Thus, the weight of a precise type of bond can be enhanced or cancelled, by changing the angle between the incident x-rays and the crystallographic axis of the sample. The linear polarization of the synchrotron radiation (continuous photon source) can be used to measure a lattice distortion induced by an interface by recording two spectra, with the x-rays coming in normal incidence (NI) (polarization of the x-rays parallel to the surface plane) or in grazing incidence (GI) (polarization of the x-rays near the perpendicular to the surface plane).

EXAFS analysis is not limited to the analysis of the first shell of neighbours. A quantitative analysis of the higher distant shell needs a multiple-scattering (MS) approach, as in the FEFF code developed by Rehr *et al* [7], since the path lengths of these single-scattering (SS) and MS contributions are similar. In order to illustrate the capabilities of the technique for the characterization of metastable thin films, EXAFS spectra have been recorded above the K edge of 3d bulk transition metal samples with different crystallographic structures, hcp cobalt, bcc iron and fcc copper, and compared with their FEFF simulations.

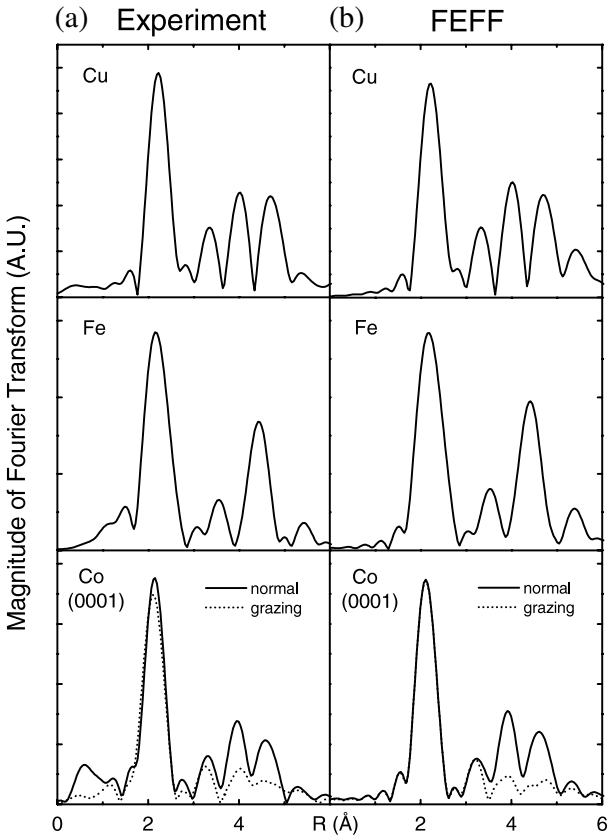

Figure 1. FT (from $k = 3.0$ to 12.6 Å^{-1}) of $k^3\chi(k)$ for (a) experimental EXAFS spectra (left-hand part) recorded at the K edge of bulk fcc Cu at 77 K, bcc Fe at 300 K and an hcp Co(0001) single crystal at 300 K. For the Co single crystal, we present two spectra, recorded in NI (solid curve) and GI (dotted curve). (b) Simulations calculated with the FEFF 6 code (right-hand part). The Debye temperature (T_{Debye}) is 343 K for Cu, 470 K for Fe and 445 K for Co. For all the simulations $S_o^2 = 0.73$.

In the hcp structure, the full point group (D_{6h}) confers to the electric dipole K-edge absorption cross section a dichroic dependence, whereas in the fcc and bcc structures, i.e. in a cubic symmetry (O_h), the electric dipole absorption cross section is isotropic [8]. Then, for cobalt, we measured this anisotropy by studying a single crystal with a (0001) surface. The spectra are recorded both in NI and in GI (the electric field is about 10° from the surface normal). The angular dependence of the SS part of the EXAFS signal is $\cos^2\alpha$ where α is the angle between the bond and the polarization direction of the x-rays (formula (2)). Then, concerning the first shell of neighbours, in GI, only the bonds out of the hexagonal planes contribute to the EXAFS signal, while in NI the bonds parallel to the hexagonal planes have a weight three times larger than the out-of-plane ones.

We have used the MS code FEFF 6.0 [7], based on the scattering path method, to simulate the EXAFS and XANES spectra recorded on bulk copper, iron and a cobalt single crystal. This version of FEFF takes the polarization of the light into account in the curved wave formalism. The single-, double-and triple-scattering processes are considered. The only free parameter is the amplitude reduction factor S_0^2, fixed at 0.7 for the three samples. The Debye temperatures are those generally assumed for these metals: 470 K for Fe, 445 K for Co and 343 K for Cu.

In figure 1, we compare the FTs of the calculated and experimental spectra. We see that the relative intensities and positions of the different peaks characteristic of a given structure (fcc for copper, bcc for iron and hcp for cobalt) are well reproduced. These well defined peaks, up to a distance of 6 Å, are due to SS on neighbours up to the sixth shell, and to MS with paths of the same lengths. In cobalt, the polarization dependence of the high distant shells is well reproduced. We can qualitatively understand the effect: among the MS paths, those that involve aligned atoms have a very high contribution (this is the well known focusing effect [9]). In an fcc structure, due to the alignment of the first and fourth neighbours, this effect is responsible for the high intensity of the third and fourth peaks. In an hcp structure, this alignment exists in the hexagonal planes. Then, the FT of the EXAFS spectrum recorded on cobalt in NI is very similar to that recorded on fcc copper. In contrast, this alignment does not exist in the direction perpendicular to the hexagonal planes. This explains why the high distant shells are strongly decreased in GI. This effect is quantitatively well reproduced by FEFF 6 and shows the ability of this code to simulate polarization-dependent EXAFS data.

Thus, EXAFS has been used to characterize metastable magnetic films. When Fe is grown on Cu(100), it tends to adopt the fcc structure of copper. Nevertheless, magnetic studies have shown that many different magnetic properties can be obtained, depending on the thickness of the films and on their growth conditions. EXAFS has been used to evidence the direct correlation between the crystallographic structure of these metastable films and their magnetic behaviour. It was shown that the films which are ferromagnetic at room temperature with PMA have an anisotropic distorted fcc structure; these films can strongly reorder and achieve a real fcc structure when their thickness is increased (above eight monolayers, ML) or when they are coated with copper [10]. Another system that presents intriguing magnetic properties and has been widely studied is the Co/Cu system. While on Cu(100) cobalt grows with an fcc-like structure [11], on Cu(111), due to the hexagonal symmetry of the surface, the stacking sequence of cobalt can be either fcc or hcp. In that case, the polarization-dependent MS analysis using the FEFF code [12] clearly shows that the films have a local hcp stacking (ABAB planes) and not the fcc stacking (ABCABC) of the substrate. Due to the selectivity of the technique, its high sensitivity was used to determine the stacking of the first interface cobalt plane [12], but also to characterize magnetic multilayers [13].

3. Tetragonal structure of Ni thin films on Cu(001)

3.1. Magnetic anisotropy in Ni/Cu(001)

For magnetic transition metal layers, the appearance of a magnetization easy axis perpendicular to the film plane (PMA) is a typical bi-dimensional effect. It has been observed in various systems, e.g. Fe/Ag(001) [14], Fe/Cu(001) [15] or Co/Pt(111) [16]. In these cases, PMA is mainly due to the truncated environment of the surface atoms (Néel anisotropy), an effect whose influence decreases, as compared to bulk effects, when the thickness of the film increases. Thus, in all the systems quoted above, a PMA was observed only up to a critical thickness, always of the order of some monolayers (ML).

A link between macroscopic quantities (like magnetic anisotropy constants) and microscopic observations (lattice distortion, local disorder, growth mode ...) is quite delicate to find [5]. Obviously, a clear explanation of the magnetic properties of thin films, as well as improvements of theoretical models, require a precise characterization of the film crystallography, with all the available experimental techniques.

This is particularly true for the Ni/Cu(001) system, considered in this section: magnetic measurements have shown that, for Ni layers thinner than 7 ML, the magnetization easy axis lies in the film plane, but switches to perpendicular to the film plane for larger thicknesses [17, 18].

PMA is observed up to 60 Å for Ni/Cu/Si(001) [19], up to 110 Å in Cu/Ni/Cu(001) sandwiches [20] and up to 140 Å in Cu/Ni/Cu/Si(001) [21, 22]. It is the epitaxial system that exhibits a perpendicular magnetization in the largest thickness range. Although all these nickel films can have different crystallographic structures, their magnetic anisotropy, whose thickness dependence is very different from those previously observed, cannot be ascribed to a surface contribution. All the models proposed to explain the thickness-dependent magnetic easy axis of the Ni/Cu(001) films have introduced a bulk [17, 20, 22] (and surface [19, 21]) magneto-elastic term, induced by a tetragonal structure of the Ni films. This structure should result from the adaptation of the Ni lattice to the Cu one. Ni and Cu are both fcc metals, with lattice parameters of, respectively, 3.52 and 3.61 Å. Ni is supposed to adopt the Cu lattice parameter parallel to the interface up to a given thickness, varying from 10 [23] to 18 Å [19]. This lateral expansion of the cell should induce a longitudinal contraction (elastic deformation), thus leading to a tetragonal structure of Ni on Cu(001). In this section, we present a SEXAFS study of Ni thin films on Cu(001). The signal is recorded in the total yield and fluorescence mode. At this energy, in these materials, the mean free path of the secondary electrons is of the order of 100 Å and that of fluorescence photons is some microns. The selectivity of the technique guarantees to probe the structure of the nickel films only, but it is characterized in its whole thickness: the contribution of each atomic plane is equivalent, rendering this structural characterization complementary to LEED studies which probe selectively the near surface planes.

3.2. SEXAFS results

We have used the linear polarization of the synchrotron radiation to measure a possible distortion of the Ni lattice, for Ni films *in situ* grown on clean Cu(001) at room temperature. For each sample, we have recorded two spectra, with the x-rays coming in NI (polarization of the x-rays parallel to the surface plane) or in GI (polarization of the x-rays at 75° from the surface plane).

The FNN shell of a Ni atom is represented in figure 2, for the supposed tetragonal structure of the thin films. Each Ni atom has 12 FNNs, four in the same (001) plane, four above (missing for the top layer) and four below (Cu atoms for the interface Ni layer). Using formula (2), a simple calculation gives that, for the FNN shell, only the eight bonds out of the (001) planes (out-of-plane bonds) contribute to the signal in GI, whereas in NI the four bonds contained in the (001) planes (in-plane bonds) and the eight out-of-plane bonds contribute with the same weight.

The main contribution to the EXAFS signal is due to this FNN shell. As can be seen in formula (1), the FNN distance appears therefore as the main frequency of the oscillations. Thus, the GI EXAFS spectrum main frequency is related to the out-of-plane FNN distance. In the NI spectrum the main frequency is the average of the in-plane and the out-of-plane FNN distances. The raw EXAFS spectra recorded in the two incidence angles on a 10 ML Ni/Cu(001) sample are presented in figure 3, together with the spectrum obtained on bulk fcc Ni. First, the general shape of the EXAFS oscillations is different in the thin film and in fcc Ni. It is particularly clear in the structures around 8570 and 8650 eV. This indicates that Ni is not fcc in the thin films. Second, the NI spectrum oscillates with a higher frequency than the GI one: the in-plane FNN distance is larger than the out-of-plane one.

More quantitatively, the out-of-plane FNN bond length ($R_{\text{out of plane}}$) and its associated mean square relative displacement ($\sigma_{\text{out of plane}}$) can be measured by fitting the experimental contribution in GI of the FNN shell with formula (1). Knowing this out-of-plane bond length, one can deduce the in-plane FNN bond length ($R_{\text{in plane}}$) and its associated mean square relative displacement ($\sigma_{\text{in plane}}$) by fitting the FNN shell contribution extracted from the NI spectrum using a (1)-type formula, containing two sine functions.

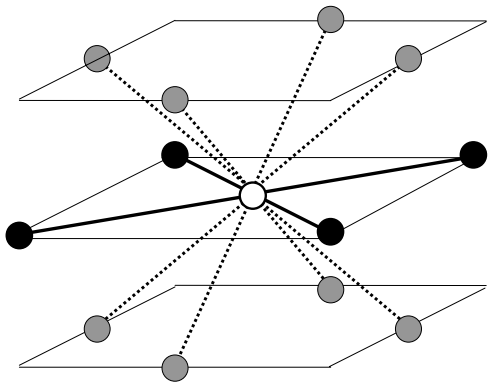

Figure 2. NN shell of a Ni atom (open circle) in a face-centred tetragonal structure. Each Ni atom has four FNNs in the same (001) plane (in-plane bonds) (closed circles), and eight out of this plane (out-of-plane bonds) (cross-hatched circles). For a face-centred tetragonal structure, the in-plane bonds are longer than the out-of-plane ones. Despite these two different distances, the 12 atoms surrounding a given Ni atom will be simply called the FNN shell in the text.

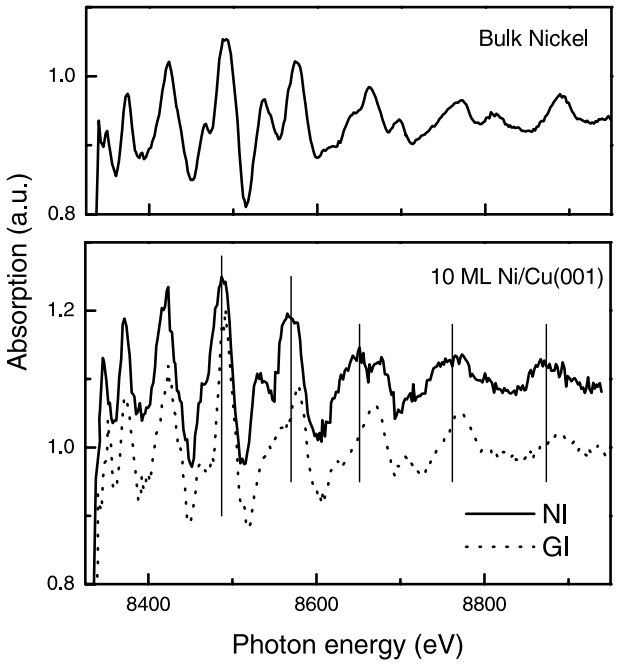

Figure 3. EXAFS spectra recorded at 77 K on a reference bulk Ni foil (top) and on a 10 ML Ni/Cu(001) film, in NI and in GI (bottom).

In the fits, the N^* were fixed to their theoretical values for a layer-by-layer growth mode. For all the studied Ni thicknesses, from 3 to 10 ML, we obtain an $R_{\text{in plane}}$ of 2.55 ± 0.01 Å, a value equal to the FNN distance in the Cu substrate (2.55 Å). $R_{\text{out of plane}}$ remains also constant with Ni thickness, with a value of 2.50 ± 0.01 Å. A complete FEFF simulation of the EXAFS spectra shows that, from 3 to 10 ML, the Ni films are in a face-centred tetragonal structure, with lattice parameters parallel to the interface $a_{\parallel} = 3.61 \pm 0.02$ Å, and perpendicular to the

interface $a_\perp = 3.46 \pm 0.04$ Å. Such a structure has already been observed in thin cobalt films deposited on Cu(001) [11]. The widths of the radial distribution and the elastic properties of the Ni films are discussed elsewhere [24].

3.3. Magneto-elastic model

Despite a quite large lattice mismatch (2.6%), the Ni tetragonal structure can be seen as an elastic deformation of the bulk cubic Ni cell, and is well described by the continuum elastic theory [24] as previously observed for thin Co films deposited on the same Cu(001) substrate [11]. Our results clearly evidence a tetragonal structure for Ni in the whole film volume, for thicknesses up to 10 ML. Together with a LEED study [23], this is the first experimental proof of this distortion which was the basis of most of the magnetic models.

In a cubic system, the magneto-elastic (ME) energy density can be estimated considering the general expression [25]

$$F_{\mathrm{ME}}^{\mathrm{cubic}} = B_1(\varepsilon_{11}\alpha_1^2 + \varepsilon_{22}\alpha_2^2 + \varepsilon_{33}\alpha_3^2) + 2B_2(\varepsilon_{12}\alpha_1\alpha_2 + \varepsilon_{23}\alpha_2\alpha_3 + \varepsilon_{31}\alpha_3\alpha_1) + \cdots \tag{3}$$

where α_i are the direction cosines of the magnetization, ε_{ij} the strains measured along the cubic axes and B_i are the ME coefficients. The nickel films have a tetragonal fcc structure which means $\varepsilon_{11} = \varepsilon_{22} > 0$, $\varepsilon_{33} < 0$ and $\varepsilon_{ij} = 0$ for $i \neq j$. Then, the difference of ME energy when the magnetization is either parallel ($\parallel$) or perpendicular ($\perp$) to the surface is

$$\Delta E_{\mathrm{ME}} = V\,\Delta F_{\mathrm{ME}} = V(F_{\mathrm{ME}}^{\perp} - F_{\mathrm{ME}}^{\parallel}) = V B_1(\varepsilon_{33} - \varepsilon_{11})$$

where V is the volume of the Ni film and $B_1 = 9.38 \times 10^7$ erg cm^{-3} for Ni [25]. Assuming a constant strain in a given range of thickness, the magneto-elastic energy, which favours a PMA in this system since $B_1 > 0$ and $\varepsilon_{33} - \varepsilon_{11} < 0$, is proportional to the film thickness. It is only in this case that, above a critical thickness, this magneto-elastic energy can compensate the surface anisotropy, which favours an in-plane magnetization [17, 23].

Our structural study, which evidences the tetragonal structure of the Ni thin films and no relaxation up to at least 10 ML, therefore validates the magneto-elastic model presented above. In the following, we will show that such an approach also allows us to understand the magnetic behaviour of nanostructures, where uniaxial relaxation of epitaxial strain occurs.

4. Strain relaxation in Fe thin films patterned by the atomic saw method

4.1. Sample preparation: the atomic saw method

50 Å thick Fe films were epitaxially grown on a MgO(001) substrate by molecular beam epitaxy at 50 °C in a vacuum of 10^{10} Torr with deposition rates from 1 to 4 Å min^{-1}. Fe epitaxially grows in a bcc-like structure on fcc MgO(001) with the relative orientation MgO(001) [010] $\parallel$ Fe(001)[110]: the bcc iron lattice is rotated by 45° with respect to the MgO lattice. The 3.8% lattice mismatch ($a_{\mathrm{Fe,bulk}} = 2.87$ and $a_{\mathrm{MgO}} = 4.21$ Å) should stretch the Fe lattice parallel to the interface. To avoid any oxidation of the Fe film, a 15 Å Pd layer was deposited on Fe. *In situ* RHEED experiments indicate that both the Fe and Pd layers present a two-dimensional growth [26, 27].

The so-called AS method was developed by Peyrade *et al* [28, 29]. It consists in applying a uniaxial compressive stress to a sample in order to favour a plastic deformation i.e. a dislocation slip through the whole system, substrate and epitaxial film. When a dislocation (respectively n dislocations) crosses the substrate–film interface, it creates a lattice shift equal to one Burger vector b (respectively $n \cdot b$). When $n \cdot b$ is larger than the film thickness, the layer is then cut into separated stripes. First applied to III–V semiconductor structures [28], this method has

been successfully used to cut Fe thin films epitaxially grown on MgO(001) into stripes and boxes [30, 31].

The plastic deformation of the whole sample induces dislocation slip throughout the MgO substrate and the thin films along the activated slip systems of the MgO substrate, which are fixed by choosing the direction of the compression axis. Indeed, plasticity calculations showed that dislocation slip induced by a compression along the MgO[100] direction is expected to cut the entire Fe film into adjacent ribbons, aligned along the MgO[010] direction, corresponding to the [110] direction in the Fe film. In practice, samples of 7 mm long by 2 mm wide and 0.5 mm thick have been plastically compressed along this compression axis, at room temperature and at a constant deformation strain rate of 1 μm min^{-1}, using an Adamel Lhomargy DY26 hard deformation machine. Fe ribbons have been made by a plastic strain of 8%. A statistical analysis of numerous atomic force microscopy pictures allowed us to evaluate accurately the influence of the plastic strain on the ribbons' width L and their relative height h [30]. The mean values obtained for L and h for a 8% plastic strain are $L = 100 \pm 50$ nm and $h = 1 \pm 0.5$ nm.

4.2. Magnetic properties

The magnetic properties of the patterned Fe films have been investigated at room temperature by magneto-optical measurements. In order to highlight any anisotropy potentially induced after the atomic saw process, we have studied the magnetization reversal for a magnetic field applied successively along the two main in-plane axes (respectively parallel and perpendicular to the ribbons). Figure 4(a) shows the magnetization reversal measured on the patterned Fe film for a magnetic field applied perpendicular to the stripes. We observe a nearly square cycle, which is the signature of an abrupt switching of the magnetization vector from the initial remanent state perpendicular to the steps to a final one in the opposite direction. Figure 4(b) displays the magnetization loop recorded for the magnetic field aligned along the stripe's edge. By increasing the magnetic field, one can observe that the magnetization gradually rotates from the initial remanent direction perpendicular to the steps to the direction parallel to the ribbons. The saturation is reached for a relatively high field close to 2400 Oe [30]. This analysis reveals a strong magnetic uniaxial anisotropy (closely dependent on the plastic strain) characterized by a magnetization easy axis perpendicular to the stripes; this is unexpected, since shape energy considerations would predict a magnetization easy axis parallel to the stripes. In fact, magneto-elastic effects due to strain relaxation induced by the structuration process can explain this magnetic anisotropy.

In the as-deposited films, the Fe bcc structure is supposed to be laterally stretched by the epitaxy on the MgO substrate. This lateral expansion should induce a longitudinal compression of the cubic unit cell, leading to a body-centred tetragonal structure, with lattice parameters a and c (see figure 5(a)). In the patterned film, the atomic saw process can then induce a relaxation of the Fe tetragonal cell perpendicular to the stripes. This would lead to a monoclinic structure schematically presented in figure 5(b), and described by three crystallographic parameters α', β' and c'.

As for the study of thin Ni films, we have used the polarization dependence of the EXAFS spectra to measure the different crystallographic parameters of these distorted structures.

4.3. EXAFS study of the as-deposited Fe film

In the supposed tetragonal structure of the as-deposited film, each Fe atom has four neighbours located at $R_3 = a$ in the same (001) plane, two neighbours on an axis perpendicular to the film plane located at a distance $R_2 = c$ and eight neighbours in the (001) planes above and

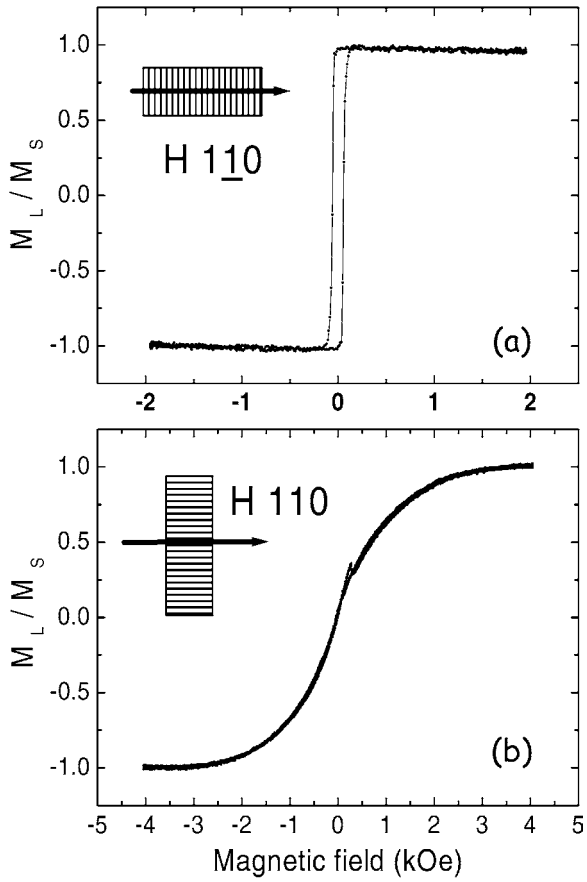

Figure 4. Magnetization hysteresis cycles measured at room temperature on the 50 Å patterned Fe film for a magnetic field applied (a) perpendicular to the ribbons, and (b) parallel to the ribbons.

below the central Fe atom, located at a distance $R_1 = \frac{1}{2}\sqrt{c^2 + 2a^2}$. A simple calculation using formula (2) shows that, in NI, the neighbours located at R_2 do not contribute to the EXAFS signal, whereas the four neighbours located at R_3 have an apparent weight of six, the eight neighbours at R_1 having an apparent weight of around eight, depending on the cubic cell tetragonalization. In GI, the neighbours located at R_3 do not contribute to the EXAFS signal, whereas the two neighbours located at R_2 have an apparent weight of six, the eight neighbours at R_1 having an apparent weight of around eight.

For this distorted bcc structure, whatever the x-ray angle of incidence, R_1, R_2 and R_3 being very close distances, there will be always two types of neighbour contributing to the NNs EXAFS signal. Unlike the case for the study of Ni/Cu(001), there is no particular x-ray angle of incidence for which a unique bond length can be isolated. A fit of the NN contribution using formula (1) would not be precise enough. We have therefore used the phase derivative method, proposed by Martens *et al* [32].

In the case where the NN contribution to the EXAFS signal $\chi_{\mathrm{NN}}(k)$ implies only two types of neighbour, located at distances R_1 and R_2, $\chi_{\mathrm{NN}}(k)$ can be written

$$\chi_{\mathrm{NN}}(k) = \frac{A_1(k)}{k}\sin(2kR_1 + \varphi(k)) + \frac{A_2(k)}{k}\sin(2kR_2 + \varphi(k))$$

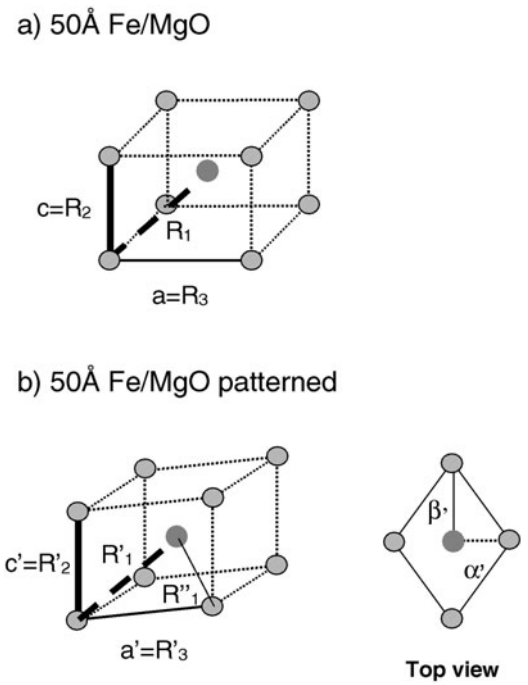

Figure 5. Schematic views of the crystallographic structures for Fe for the Fe/MgO films: (a) in the as-deposited film and (b) in the film patterned with the atomic saw method.

or

$$\chi_{\mathrm{NN}}(k) = \mathrm{Im}\left(\frac{A_1(k)}{k}\exp \mathrm{i}(2kR_1 + \varphi(k)) + \frac{A_2(k)}{k}\exp \mathrm{i}(2kR_2 + \varphi(k))\right)$$

with $A_i(k) = \frac{N_i^*}{R_i^2}B_i(k)\mathrm{e}^{-2k^2\sigma_i^2}$ so that, finally,

$$\chi_{\mathrm{NN}}(k) = \frac{\tilde{A}(k)}{k}\sin(2k\tilde{R} + \tilde{\Phi}(k))$$

with

$$\tilde{A}(k) = A_1(k)\sqrt{1 + \left(\frac{A_2(k)}{A_1(k)}\right)^2 + 2\frac{A_2(k)}{A_1(k)}\cos(k\Delta R)}$$

$$\tilde{\Phi}(k) = \varphi(k) + \tan^{-1}\left(-\frac{A_1(k) - A_2(k)}{A_1(k) + A_2(k)}\tan(k\Delta R)\right)$$

$$\tilde{R} = \frac{R_1 + R_2}{2} \qquad \text{and} \qquad \Delta R = R_2 - R_1.$$

$\tilde{\Phi}(k)$ is the χ_{NN} total phase. Under some assumptions (a linear dependence in k of $\varphi(k)$, and the same width of the radial distribution function σ for the two shells), one can show that kinks occur in this total phase $\tilde{\Phi}(k)$ for the k values given by [32]

$$k_{2n+1} \approx \frac{(2n+1)\pi}{2\Delta R} \tag{4}$$

linked to the ΔR value. The kink position is located by calculating the derivative of the total phase with respect to k. An example is given in figure 6 for bulk bcc Fe (FNNs at

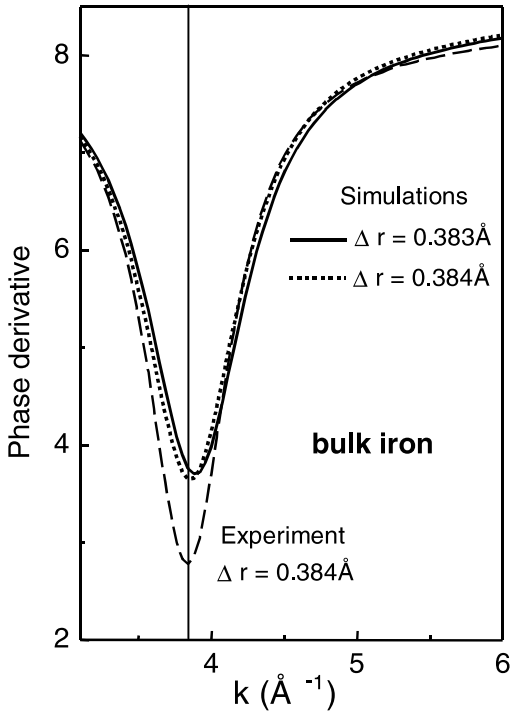

Figure 6. Experimental phase derivative of bulk Fe (dashed curve), compared with two simulations calculated using the FEFF code for two Fe structures with a lattice parameter $a = 2.866$ Å ($\Delta R = 0.384$ Å) (dotted curve) and $a = 2.86$ Å ($\Delta R = 0.383$ Å) (full curve).

$R_1 = 2.482$ Å and second NNs at $R_2 = 2.866$ Å, $\Delta R = 0.384$ Å). We have extracted the NN contribution from an experimental EXAFS spectrum and calculated its total phase derivative. One observes a kink located at $k = 3.86$ Å^{-1}, which would give, using formula (4), a ΔR value of 0.406 Å, quite different from the real value of 0.384 Å. This difference is due to the strong assumptions made to derive formula (4) (mainly the linear dependence in k of $\varphi(k)$). One can modify formula (4) to improve its precision [33], but it will always give only an approximate value of ΔR.

A precise way to obtain ΔR is to compare the experimental phase derivative with a theoretical calculation done with the FEFF7 code [7] on bulk Fe. This is done in figure 6, with a simulation calculated for a lattice parameter $a = 2.87$ Å. The general shape of the experimental phase derivative and its minimum position are very well reproduced. Let us point out that the phase derivative calculated for a slightly different Fe bcc structure ($a = 2.86$ Å, $\Delta R = 0.383$ Å) shows a minimum at a significatively different k position ($\Delta k = 0.04$ Å^{-1}). This demonstrates the accuracy of the method for the determination of ΔR.

This method was applied for the structure determination of the as-deposited film. Figure 7(a) shows the experimental phase derivative calculated for the EXAFS spectra recorded in NI and in GI. In the case of a tetragonal structure, using the notations of figure 5(a), we have $\Delta R_{\mathrm{NI}} = a - R_1$ and $\Delta R_{GI} = c - R_1$. With $a > c$, one obtains $\Delta R_{\mathrm{NI}} > \Delta R_{\mathrm{GI}}$, and therefore, according to formula (2), a kink position at a smaller k value in NI than in GI. This is what we clearly observe; this evidences the tetragonal structure of the as-deposited Fe film. We have used an improved formula (2) [33] to obtain approximate values of ΔR_{NI} and ΔR_{GI}, and then

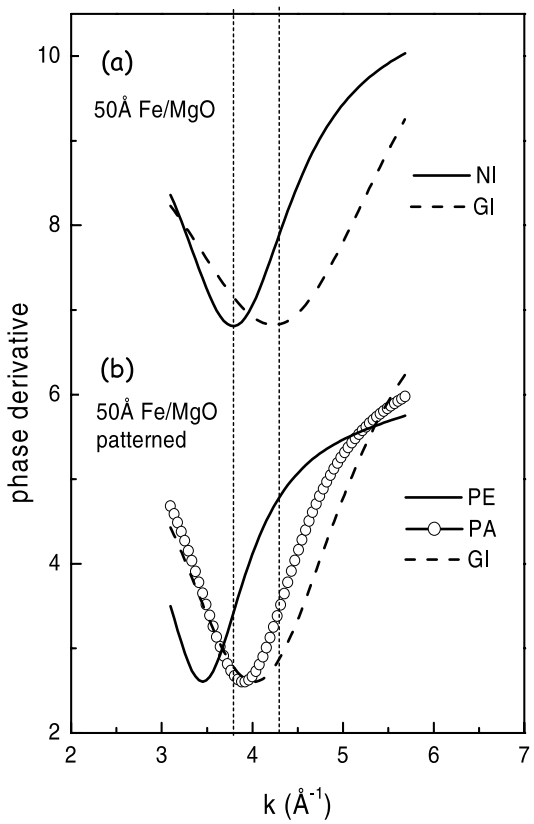

Figure 7. Experimental phase derivatives (a) for the as-deposited Fe film in NI (full curve) and GI (dashed curve) and (b) for the patterned film with the polarization of the x-rays perpendicular to the stripes (full curve), parallel to the stripes (open circles) and in GI (dashed curve).

refined the structure in FEFF7 simulations, by successive 0.01 Å steps for the two parameters a and c. The best agreement between experiment and simulations is found for $a = 2.92$ Å and $c = 2.82$ Å.

As was supposed above, in the as-deposited film, Fe is in a tetragonal structure, resulting from an epitaxialy strained bcc structure.

4.4. EXAFS study of the patterned Fe film

In the patterned Fe film, the Fe structure is expected to be monoclinic, and described by three crystallographic parameters α', β' and c' (see figure 5(b)). In this structure, the shell constituted by the eight atoms at $R_1 = \frac{1}{2}\sqrt{c^2 + 2a^2}$ in the stretched bcc structure is now split into two shells of four atoms in the (001) planes above and below the central Fe atom, located at distances $R'_1 = \frac{1}{2}\sqrt{c'^2 + 4\beta'^2}$ and $R''_1 = \frac{1}{2}\sqrt{c'^2 + 4\alpha'^2}$. Concerning the next neighbour shells, each Fe atom has four neighbours located at $R'_3 = a' = \sqrt{\alpha'^2 + \beta'^2}$ in the same (001) plane, and two neighbours on an axis perpendicular to the film plane located at a distance $R'_2 = c'$.

For these patterned samples, we have recorded three absorption spectra: a GI spectrum, with the linear polarization of the x-rays perpendicular to the film plane, and two NI spectra, with the linear polarization of the x-rays parallel to the film plane, but either parallel (PA) or

perpendicular (PE) to the stripes. One can once again estimate the apparent weight of each type of bond using formula (1). In GI, the neighbours located at R'_3 do not contribute to the EXAFS signal; the NN contribution will be a mixing of three other shells' contributions. In NI, with the polarization vector along the stripes, the neighbours located at R'_2 and R''_1 do not contribute to the EXAFS signal; the contribution of the NNs shell will be due to shells located at R'_3 and R'_1. On the other hand, in NI, but with the polarization vector perpendicular to the stripes, only the neighbours located at R'_3 and R''_1 contribute to the EXAFS signal. For this distorted bcc structure, whatever the x-ray angle of incidence, the NN contribution to the EXAFS signal involves two or three different close shells.

We have used the same phase derivative method to analyse the data. Figure 7(b) displays the experimental phase derivatives obtained for the three different x-ray incident angles: they are all strongly different from the data recorded on the as-deposited film, displaying the structural rearrangement induced by the atomic saw process. The two NI spectra, recorded with the polarization either parallel (PA) or perpendicular (PE) to the Fe ribbons, present minima located at different k values, denoting a non-square symmetry of the surface lattice. According to our notations, the bond length differences involved for each polarization direction are

$$\Delta R_{\mathrm{PE}} = R'_3 - R''_1$$
$$\Delta R_{\mathrm{PA}} = R'_3 - R'_1$$
$$\Delta R_{\mathrm{GI}} \approx R'_2 - \tfrac{1}{2}(R'_1 + R''_1).$$

As for the study of the as-deposited film, approximate values of these different ΔR are derived from the minimum k position using an improved formula (3) [33]; the final α', β' and c' crystallographic parameters are obtained by comparing the experimental curves with FEFF7 simulations. The best agreement is found for $\alpha' = 2.02$ Å, $\beta' = 2.07$ Å and $c' = 2.83$ Å, with an accuracy of about 0.01 Å. These values have to be compared with the crystallographic parameters of the as-deposited films ($a = 2.92$ Å (i.e. $\alpha = \beta = 2.06$ Å) and $c = 2.82$ Å).

This result evidences a monoclinic structure of the patterned Fe film. As it was supposed, the effect of the AS process is mainly to relax the epitaxial strain perpendicular to the stripes. Thus, the structure is also slightly relaxed perpendicular to the film plane ($c' > c$). The uniaxial relief δ of the strain field along the direction perpendicular to the stripes can be written

$$\delta = \frac{\beta' - \alpha'}{\alpha'} = 2.5 \pm 0.6\%.$$

4.5. Magneto-elastic model

The magneto-elastic energy in a cubic structure is given by formula (3). Using the coordinates in the standard Fe[100] basis, the magneto-elastic energy density can be expressed in the two symmetry directions, perpendicular to the stripes ([1$\bar{1}$0] direction), or parallel to them ([110] direction):

$$F^{\perp}_{\mathrm{ME}} = \frac{B_1}{2}(\varepsilon_{11} + \varepsilon_{22}) - B_2\varepsilon_{12} \qquad \text{and} \qquad F^{\parallel}_{\mathrm{ME}} = \frac{B_1}{2}(\varepsilon_{11} + \varepsilon_{22}) + B_2\varepsilon_{12}.$$

The energy difference between the two magnetization directions can be written

$$\Delta F_{\mathrm{ME}} = F^{\perp}_{\mathrm{ME}} - F^{\parallel}_{\mathrm{ME}} = -2B_2\varepsilon_{12}.$$

Since $\varepsilon_{12} = \delta/2$ and with $B_2 = 7.62 \times 10^7$ erg cm^{-3} [34], we have

$$\Delta F_{\mathrm{ME}} = -B_2\delta = -1.9 \times 10^6 \text{ erg cm}^{-3}.$$

This negative value shows that a magnetization vector perpendicular to the ribbons minimizes the magneto-elastic energy, as observed in the magneto-optical measurements. The anisotropy

field H_a, given by $H_a = 2\Delta E_{\mathrm{ME}}/M_S$, is roughly equal to 2250 Oe, a value very close to the one determined experimentally (2400 Oe), which proves the validity of this simple magneto-elastic model.

A switching of the magnetization easy axis was also reported for Fe deposits on W(110) [35]. The authors showed that an annealing of the Fe films allowed creation of elongated islands with a magnetization easy axis different from the one of the continuous as-deposited film. But, in this latest case, the switching seems to be due to changes in the film morphology and not to structural effects, as discussed here.

5. Cobalt films deposited on the stepped Cu(11 n) surfaces

5.1. Magnetic characterization

Cobalt layers grown on stepped copper surfaces are at the origin of the discovery of spectacular phenomena of in-plane magnetization reversal [36]. It is well known that magnetic films grown on vicinal surfaces show a step-induced twofold magnetic anisotropy which favours either a parallel alignment of the magnetization and the step edges (as on Co/Cu(11n) [37–41]) or a perpendicular one [42].

Since an in-plane magnetic anisotropy with fourfold symmetry is found for cobalt grown on flat Cu(001) [43], the origin of the uniaxial anisotropy in Co/Cu(11n) is currently believed to arise from missing bonds at step edges (Néel-type anisotropy [38]) and/or strain in the film (ME anisotropy [39]) but without being clearly evidenced. To distinguish the two contributions, a precise knowledge of the atomic structure and the morphology of the films are required.

In order to test the role of the step density, cobalt films grown on both Cu(115) and Cu(1 1 11) surfaces are presented. The high step density allows expectation of a large magnetic anisotropy [40]. We combine magnetic anisotropy measurements by the surface magneto-optical Kerr effect (SMOKE) with a morphological and structural analysis by STM and SEXAFS respectively. These three techniques were performed *in situ* in an ultra-high vacuum environment on the very same samples. Cobalt was deposited at room temperature in NI.

The Cu(115) and Cu(1 1 11) surfaces are vicinal surfaces of Cu(001): they consist respectively of 2.5 and 5.5 atom wide (001) terraces separated by (111)-type steps running along the $[\bar{1}10]$ direction. On the clean substrates, STM images show well defined and equally spaced steps (figures 9(a) and (b)).

The magnetic anisotropy on Co/Cu(11n) films was investigated by SMOKE at 300 K in a longitudinal geometry [44]. The sample azimuth could be varied to orient the in-plane applied magnetic field in any direction from perpendicular to parallel to the step edges. In figure 8, representative SMOKE curves with the applied field in the (115) plane and parallel (in the $[\bar{1}10]$ direction) or perpendicular to the step edges (in the $[\bar{5}\bar{5}2]$ direction) are shown for an 8 ML Co/Cu(115) film. For all samples, the hysteresis loop shows no remanence (hard axis) when the field is applied perpendicular to the steps, whereas for the field aligned along the steps a square loop is obtained (easy axis), as observed earlier [36, 41]. This magnetic behaviour is consistent with the presence of a biaxial anisotropy (K_4) and uniaxial anisotropy (K_u).

Assuming that the magnetization is kept in the (001) plane, the free magnetic energy can be written as [45]

$$E(\varphi) = K_u \sin^2(\varphi) + K_4/4 \cos^2(2\varphi) - MH \cos(\varphi - \theta)$$

where φ is the angle of the magnetization (M) with respect to the $[\bar{1}10]$ direction, and θ the angle between the applied field (H) and the $[\bar{1}10]$ direction. The biaxial anisotropy constant K_4 has been found to be negative for Co/Cu(001) films [43] i.e. the easy directions are parallel

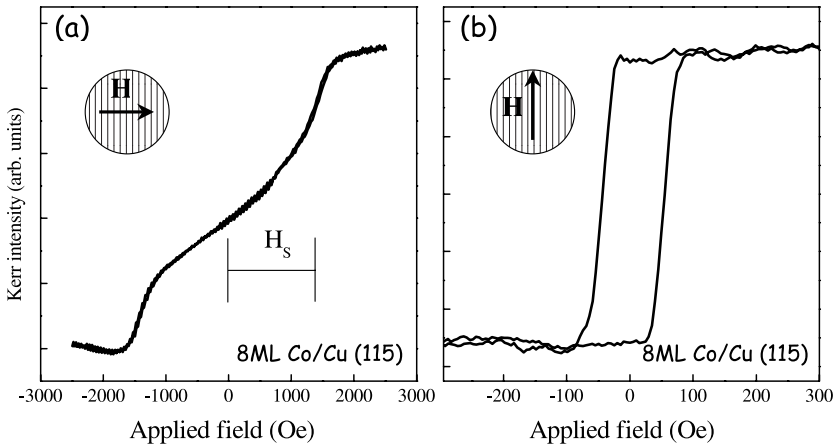

Figure 8. Magnetization in-plane hysteresis loops measured by SMOKE, at room temperature, on an 8 ML Co/Cu(115) film, for a magnetic field applied in the (115) plane and (a) perpendicular to the step edges (in the $\bar{5}\bar{5}2$ direction, hard axis), and (b) parallel to the step edges (in the $\bar{1}10$ direction, easy axis).

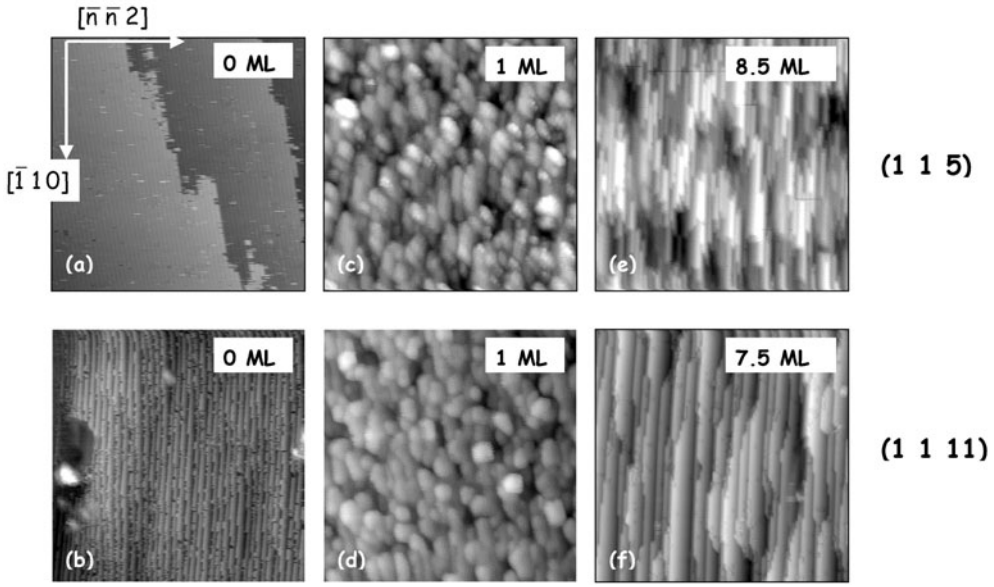

Figure 9. STM images at different coverages for Co/Cu(1 1 $\bar{5}$) (a), (c), (e) and Co/Cu(1 1 11) (b), (d), (f) films. The step edge and easy magnetization axis ($\bar{1}10$ direction) is along the vertical axis and the $\bar{n}\bar{n}2$ direction (ascending step direction) is along the horizontal axis. Image size is 512×512 Å^2. STM images are for clean surfaces (a), (b), 1 ML (c), (d) and 8 ML (e), (f) thick cobalt films.

and perpendicular to the $[\bar{1}10]$ direction. Furthermore, K_u is positive, leading to an easy axis of the uniaxial anisotropy in the step edge direction ($[\bar{1}10]$). The measurement of the shift field (H_s) (see figure 8(a)) of the split loop together with the slope at zero field allow the calculation of the uniaxial and biaxial anisotropy constants [46]. Using this model, we have calculated the anisotropy constants K (K_u and K_4) for the different samples. K can be separated into a

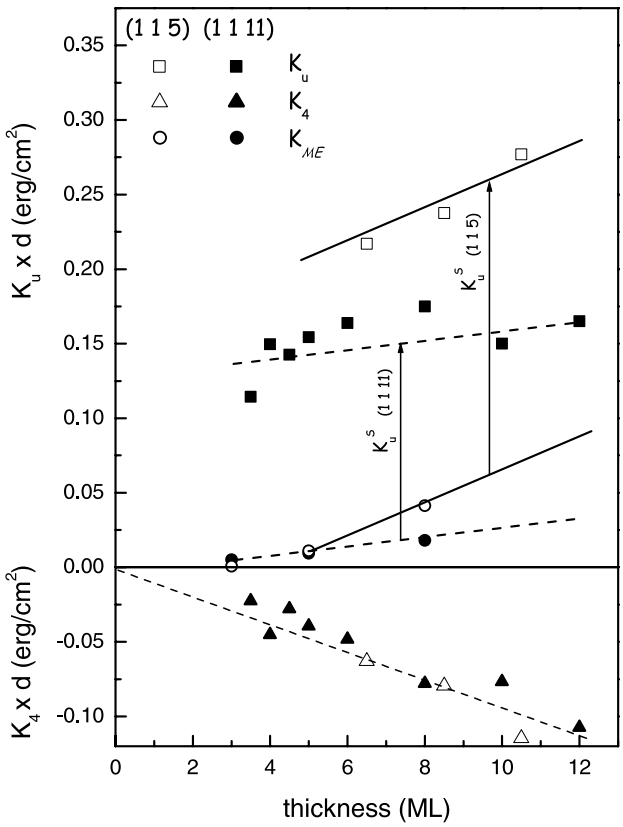

Figure 10. Values of in-plane anisotropy constants multiplied by the Co film thickness d, as a function of d: experimental values of in-plane anisotropy constants (squares K_u, triangles K_4), and calculated values of the ME anisotropy (circles K_{ME}) with structural parameters deduced from SEXAFS experiment. The open symbols concern cobalt films grown on the Cu (1 1 5) surface and the dark symbols concern the (1 1 11) surface. The arrows indicate the values of the surface contribution to the in-plane anisotropy, K_u^S (see text).

volume term K^b and a surface term K^s: $K = K^b + K^s/d$, where d is the film thickness. In figure 10, the values of $K \times d$ are plotted as a function of d. $K_4 \times d$ is almost proportional to d: it shows a small surface contribution, and the slope of the curve gives a K_4^b value of about -5.5×10^5 erg cm^{-3} in fair agreement with data previously obtained on Cu(001) [43]. Otherwise, $K_u \times d$ is about 0.25 erg cm^{-2} for Cu(1 1 5), 0.15 erg cm^{-2} for Cu(1 1 11) and K_u seems to have both a surface and a volume contribution. As expected, the uniaxial anisotropy becomes higher as the step density is increased. The behaviour and origin of K_u will be discussed after the description of the structure and the morphology of the cobalt film.

5.2. STM determination of the film morphology

Typical STM images recorded at 300 K before and after cobalt deposition are shown in figure 1. For the clean substrates (figures 9(a) and (b)), STM images show large domains of well defined equally spaced steps. At the very first stage of Co growth (0.01 ML, not shown here), we observe a high meandering of steps on Cu(1 1 11) and a decrease of the size of well ordered domains on Cu(1 1 5). A simple growth of cobalt islands or direct exchange between Co and

Cu atoms cannot explain these morphologies. The number of displaced atoms is much larger than the number of deposited Co atoms [47]. On the two surfaces, collective displacement of Cu atoms takes place, as observed on Co/Cu(1 1 17) [48]. Between 1 and 3 ML nearly isotropic islands (typical size 6–7 nm) are observed (figures 9(c) and (d)). Upon increasing the thickness, the islands coalesce and form relatively straight steps aligned with the $[\bar{1}10]$ axis. This coalescence is not complete at 5 ML and some deep holes remain on the surface. For 8 ML (figures 9(e) and (f)) the typical length of straight steps increases but the distribution of the terrace width is wider than on the clean substrate. Then the Co films do not reproduce the vicinal topography of the substrate, showing that the growth is not layer-by-layer in agreement with previous experiments on other Cu vicinal surfaces [48]. The growth is then different from the one observed on flat Cu(001) where a layer-by-layer growth is identified above 2 ML [49] and where significant intermixing occurs only below 2 ML [50]. Moreover, to understand the magnetic properties in stepped thin films, in the frame of the Néel model, the number of atoms at step edges is needed. The STM experiments appear as essential, since they show that the surface morphology strongly evolves with film thickness.

5.3. Structural characterization by EXAFS

A precise knowledge of the crystallographic structure of the films is also mandatory to explain the magnetic properties of Co films, and SEXAFS experiments were carried out at the Co K edge (7709 eV) at 77 K for films between 3 and 8 ML. Due to the lattice mismatch between Co and Cu, for Co/Cu(11 n) films, we expect a face-centred tetragonal structure similar to that of Co films grown on flat Cu(001) [11]. Moreover, due to the lower symmetry of the substrate, three different NN bond lengths around Co atoms can be expected: R_{PA} (bonds in the terrace plane and parallel to the step edge), R_{PE} (bonds in the terrace plane and perpendicular to the step edge), and R_{out} (out-of-plane bonds) [47]. If this structural distortion exists, an ME contribution to the anisotropy may appear.

Three spectra using a linear polarization of the x-rays oriented successively along $[\bar{1}10]$, [110] and [001] were recorded on the samples, allowing the measure of the different bond lengths. Although the expected anisotropy, with three different symmetry axes, is similar to that of the patterned Fe films presented above, the EXAFS analysis is much simpler since, in an fcc-like structure, the first shell of neighbours is well separated from the higher distant ones and its contribution is well identified in the EXAFS spectra. For the simulation of the EXAFS spectra, a slightly distorted face-centred tetragonal structure ($R_{\mathrm{PA}} \neq R_{\mathrm{PE}}$) for Co and no intermixing are assumed. The simulation is done in a polarization-dependent MS approach by fitting the spectra up to the fourth shell of neighbours with the FEFFIT code [51]. The best agreement was achieved for the parameters summarized in table 1. For all films, isotropic values for the mean NN distances in the terrace plane ($R_{\mathrm{PA}} = R_{\mathrm{PE}}$) are obtained. Therefore, the steps do not induce any in-plane structural anisotropy.

For films grown on Cu(1 1 11), the local atomic structure is very similar to that of Co/Cu(001) where the cobalt film is tetragonally distorted [11] with a lattice parameter parallel to the surface equal to the Cu one (2.55 Å) and R_{out} equal to 2.50 Å. In contrast, for 3 ML Co/Cu(1 1 5), the structure is completely isotropic: $R_{\mathrm{PA}} = R_{\mathrm{PE}} = R_{\mathrm{out}} = 2.53$ Å (a value between Cu and Co bulk ones). This isotropic local structure is probably due to a copper–cobalt intermixing favoured by the high step density; STM images have shown a very high mobility of copper atoms, at the very first stages of cobalt growth. For thicker films on Cu(1 1 5), Co adopts a slightly anisotropic face-centred tetragonal structure. For all the films, the NN distances for the two in-plane directions are equal: there is no anisotropic in-plane strain relaxation.

Table 1. Structural parameter results of least-squares fits of the EXAFS spectra for different thickness of cobalt films grown on the stepped Cu(1 1 5) and Cu(1 1 11) surfaces. R_{PA} and R_{PE} are the cobalt NN distances determined for bonds parallel to the (001) terrace planes either parallel (PA) or perpendicular (PE) to the step edges. R_{out} is the NN distance for out of plane bonds.

Cobalt thickness		R_{PA} (Å)	R_{PE} (Å)	R_{out} (Å)
3 ML	Cu(115)	2.54 ± 0.01	2.53 ± 0.01	2.53 ± 0.01
	Cu(1111)	2.56 ± 0.01	2.56 ± 0.01	2.52 ± 0.01
5 ML	Cu(115)	2.53 ± 0.01	2.53 ± 0.01	2.52 ± 0.01
	Cu(1111)	2.56 ± 0.01	2.55 ± 0.01	2.52 ± 0.01
8 ML	Cu(115)	2.54 ± 0.01	2.54 ± 0.01	2.51 ± 0.01
	Cu(1111)	2.55 ± 0.01	2.55 ± 0.01	2.51 ± 0.01

5.4. Origin of the magnetic anisotropy

Then, the magnetic properties can be discussed in the light of the morphological and structural data. The SEXAFS results show that the step-induced anisotropy cannot be explained by an in-plane (001) structural anisotropy as supposed earlier [39]. Hence, the uniaxial anisotropy must be interpreted considering mainly the film morphology.

Nevertheless, since on a stepped surface the high density crystallographic planes (here (001)) are not parallel to the average surface (11 n) plane, the tetragonal distortion of the cobalt films, which is perpendicular to the (001) planes, induces some anisotropy in the (11 n) planes. This ME contribution to the anisotropy can be estimated considering the general expression for a cubic system given in formula (3).

SEXAFS experiments have shown that $\varepsilon_{ij} = 0$ for $i \neq j$ and $\varepsilon_{11} = \varepsilon_{22}$. We have calculated the difference of ME energy when the magnetization is either parallel to the steps ($\parallel = [\bar{1}10]$) or perpendicular to them ($\perp = [\bar{n}\bar{n}2]$):

$$\Delta F_{ME} = F_{ME}^{\perp} - F_{ME}^{\parallel} = B_1(\varepsilon_{33} - \varepsilon_{11}) \sin^2 \alpha,$$

ΔF_{ME} is the ME contribution to the volumic part of K_u, where α is the miscut of the (11n) surface with respect to the (001) surface ($\alpha = 7.3°$ for Cu(1 1 11) and $\alpha = 15.8°$ for Cu(1 1 5)). Figure 10 displays $\Delta F_{ME} \times d$ calculated with $B_1 = -9.2 \times 10^7$ erg cm^{-3} [25] and ε_{ij} deduced from SEXAFS experiments (assuming a lattice parameter for fcc Co of $a = 3.543$ Å [11]). For both systems, the thickness variation of $\Delta F_{ME} \times d$ is roughly parallel to that of the experimental $K_u \times d$, with a higher slope for the Cu(1 1 5) system. So the bulk contribution to K_u is mainly due to the tetragonal distortion of the films. Considering the absolute values, this bulk ΔF_{ME} contribution is about one-tenth of the experimental value of K_u. So, it is clear that the major contribution to K_u is a 'surface-like' one, K_u^S (figure 10). The experimental values of K_u^S are of the order of 0.20 erg cm^{-2} for Co/Cu(1 1 5) and 0.13 erg cm^{-2} for Co/Cu(1 1 11).

We can now evaluate the contribution to K_u^S arising from the surface morphology of the film, i.e. the distribution of missing bonds. This contribution can be estimated within the Néel model [53]. The magneto-crystalline anisotropy of a Co atom and its neighbour i is written as $w_i = l_{Co}(\cos^2 \theta_i - 1/3)$ with θ_i the angle between the bond i and the magnetization. The total Néel energy is $W_{Neel} = \frac{1}{2} \sum_i w_i$. The Néel coefficient, l_{Co}, can be estimated from the ME coefficients for fcc Co [25, 53]: $l_{Co} = -6.52 \times 10^7$ erg cm^{-3}. Considering only the surface of the film, we have calculated the contribution of missing bonds to the magnetic uniaxial anisotropy, using the value of the surface Néel coefficient for a (001) surface, $l_{Co}^S = d_{(001)} \times l_{Co} = -1.12$ erg cm^{-2} where $d_{(001)}$ is the distance between the cobalt (001) planes. Assuming perfect cobalt vicinal surfaces, we find a surface magneto-crystalline

uniaxial anisotropy:

$$\Delta W_{\text{Neel}} = W_{\text{Neel}}^{\perp} - W_{\text{Neel}}^{\parallel} = -0.123 \times l_{\text{Co}}^{S} = 0.14 \text{ erg cm}^{-2} \text{ for a perfect Co/Cu(1 1 5) surface}$$
$$= -0.074 \times l_{\text{Co}}^{S} = 0.08 \text{ erg cm}^{-2} \text{ for a perfect Co/Cu(1 1 11) surface .}$$

These values represent roughly two-thirds of the experimental values of K_u^S.

Since STM images show that the step edges are not perfectly straight, we have calculated the Néel anisotropy taking into account atomic kinks along steps (note that in this first neighbour Néel model, neither multiple steps nor faceting change the value of the anisotropy). The distances between kinks are evaluated from figure 9 to be about 30 Å for 8 ML Co/Cu(1 1 5) and 34 Å for 8 ML Co/Cu(1 1 11) which gives respectively $\Delta W_{\text{Neel}} = -0.106 \times l_{\text{Co}}^{S} = 0.12$ erg cm^{-2} and $\Delta W_{\text{Neel}} = -0.066 \times l_{\text{Co}}^{S} = 0.075$ erg cm^{-2}. These values are close to the ones calculated for straight step edges. The reduction of the anisotropy induced by the presence of the kinks is noticeable only for the thinner films (below 5 ML) where the kink density is much higher.

The calculated Néel surface contribution accounts for about 50% of the uniaxial anisotropy (in terms of $K \times d$) whereas the ME energy accounts for about 10–15% only. The missing part might have two contributions: in the Néel model, we have not considered the Co/Cu interface anisotropy, since it is supposed to have a much smaller effect than the free surface, and, in the Néel model, the sum of the magnetic pair energy is limited to the first neighbours, though the interaction is long ranged. We have also to add the effect of shape anisotropy induced by the morphology of the cobalt films, which could be of the same order of magnitude as the Néel anisotropy [54].

In summary, we have shown that the uniaxial anisotropy of Co films grown on vicinal Cu(115) and Cu(1 1 11) surfaces is not due to an in-plane anisotropic step-induced strain relaxation. SEXAFS measurements of the strain in the different directions, in plane and out of plane, show that ME effects only contribute to about 10% to the total anisotropy. STM measurements were used to estimate the Néel surface anisotropy, which turned out to be the main contribution to the uniaxial anisotropy, in agreement with previous assumptions on such systems [38].

6. Conclusion

For a correct description of unusual magnetic properties of thin films and nanostructures, both a local crystallographic and morphological characterization of the systems are needed: through the spin–orbit interaction and shape effects, any crystallographic anisotropy induces magnetic anisotropy. In thin Ni films deposited on Cu(001) as well as in Fe nanostructures, we have shown that a precise structural characterization allows understanding of the magnetic properties: in both cases, these properties are explained using simple magneto-elastic models. In contrast, for cobalt films grown on Cu vicinal surfaces, SEXAFS results rule out the existence of any in-plane strain relaxation. In this case, the origin of the uniaxial magnetic anisotropy is mainly a Néel type surface anisotropy that can be estimated from STM observation of the surface morphology.

References

[1] Gay J G and Richter R 1986 *Phys. Rev. Lett.* **56** 2728
[2] Allenspach R, Stampanoni M and Bischof A 1990 *Phys. Rev. Lett.* **65** 3344
[3] Chappert C and Bruno P 1988 *J. Appl. Phys.* **64** 5736
[4] Pommier J, Meyer P, Penissard G, Bruno P, Ferré J and Renard D 1986 *Phys. Rev. Lett.* **56** 2728

[5] Bruno P and Renard J-P 1989 *Appl. Phys.* A **49** 499
Bruno P 1989 *Phys. Rev.* B **39** 865
[6] Sayers D E, Stern E A and Lytle F W 1971 *Phys. Rev. Lett.* **27** 1204
[7] Rehr J J, Mustre de Leon J, Zabinski S I and Albers R C 1991 *J. Am. Chem. Soc.* **113** 5135
Mustre de Leon J, Rehr J J, Zabinsky S I and Albers R C 1991 *Phys. Rev.* B **44** 4146
Rehr J J, Alberts R C and Zabinsky S I 1992 *Phys. Rev. Lett.* **69** 3397
[8] Brouder C 1990 *J. Phys.: Condens. Matter* **2** 701
[9] Lee P A and Pendry J B 1975 *Phys. Rev.* B **11** 2795
[10] Magnan H, Chandesris D, Villette B, Heckmann O and Lecante J 1991 *Phys. Rev. Lett.* **67** 859
[11] Heckmann O, Magnan H, Le Fèvre P, Chandesris D and Rehr J J 1994 *Surf. Sci.* **312** 62
[12] Le Fèvre P, Magnan H, Heckmann O, Briois V and Chandesris D 1995 *Phys. Rev.* B **52** 11462
[13] Pizzini S, Baudelet F, Chandesris D, Fontaine A, Magnan H, George J M, Petroff F, Barthelemy A, Fert A, Loloee R and Schroeder P A 1992 *Phys. Rev.* B **46** 1253
[14] Heinrich B, Urquhart K B, Arrot A S, Cochran J F, Myrtle K and Purcell S T 1987 *Phys. Rev. Lett.* **59** 1756
Koon N C, Jonker B T, Volkening F A, Krebs J J and Prinz G A 1987 *Phys. Rev. Lett.* **59** 2463
Araya-Pochet J, Ballentine C A and Erskine J L 1988 *Phys. Rev.* B **38** 7846
[15] Pescia D, Stampanoni M, Bona G L, Vaterlaus A, Willis R F and Meier F 1987 *Phys. Rev. Lett.* **58** 2126
Liu C, Moog E R and Bader S D 1988 *Phys. Rev. Lett.* **60** 2422
[16] Allenspach R 1994 *J. Magn. Magn. Mater.* **129** 160
Thiele J, Boeglin C, Hricovini K and Chevrier F 1996 *Phys. Rev.* B **53** 11934
[17] Schulz B and Baberschke K 1994 *Phys. Rev.* B **50** 13467
Schulz B, Schartzwald R and Baberschke K 1994 *Surf. Sci.* **307–309** 1102
[18] Huang F, Kief M T, Mankey G J and Willis R F 1994 *Phys. Rev.* B **49** 3962
[19] Bochi G, Ballentine C A, Inglefield H E, Thompson C V, O'Handley R C, Hug H, Stiefel B, Moser A and Güntherodt H-J 1995 *Phys. Rev.* B **52** 7311
[20] Jungblut R, Johnson M T, aan de Stegge J, Reinders A and den Broeder F J A 1994 *J. Appl. Phys.* **75** 6424
[21] Bochi G, Ballentine C A, Inglefield H E, Thomson C V and O'Handley R C 1996 *Phys. Rev.* B **53** 1729
[22] Naik R, Kota C, Payson J S and Dunifer G L 1993 *Phys. Rev.* B **48** 1008
[23] Müller S, Schulz B, Kostka G, Farle M, Heinz K and Baberschke K 1996 *Surf. Sci.* **364** 235
Platow W, Bovensiepen U, Poulopoulos P, Farle M, Baberschke K, Hammer L, Walter S, Müller S and Heinz K 1999 *Phys. Rev.* **59** 12641
[24] Le Fèvre P, Magnan H and Chandesris D 1999 *Eur. Phys. J.* B **10** 555
[25] Sanders D 1999 *Rep. Prog. Phys.* **62** 809
[26] Durand O, Childress J R, Galtier P, Bisaro R and Schuhl A 1995 *J. Magn. Magn. Mater.* **145** 111
[27] Childress J R, Kergoat R, Durand O, George J M, Galtier P, Miltat J and Schuhl A 1994 *J. Magn. Magn. Mater.* **130** 13
[28] Peyrade J P, Voillot F, Goiran M, Atmany H and Rocher A 1992 *Appl. Phys. Lett.* **60** 2481
[29] Goiran M, Guasch C, Voillot F, Carles R, Peyrade J P, Bedel E and Munoz-Yague A 1993 *Europhys. Lett.* **23** 647
[30] Jaffrès H, Ressier L, Postava K, Schuhl A, Nguyen Van Dau F, Goiran M, Redoulès J P, Peyrade J P and Fert A R 1998 *J. Magn. Magn. Mater.* **184** 19
[31] Jaffrès H, Ressier L, Peyrade J P, Fert A R, Gogol P, Thiaville A, Schuhl A and Nguyen F 1998 *J. Appl. Phys.* **84** 4375
[32] Martens G, Rabe P, Schwentner N and Werner A 1977 *Phys. Rev. Lett.* **39** 1411
Jiang D T, Crozier E D and Heinrich B 1991 *Phys. Rev.* B **44** 6401
[33] Jaffrès H, Le Fèvre P, Magnan H, Midoir A, Chandesris D, Ressier L, Schuhl A, Nguyen Van Dau F, Goiran M, Peyrade J P and Fert A R 2000 *Phys. Rev.* B **61** 14628
[34] Bruno P 1993 Magnetismus von Festkörpen und Grenzflächen *Ferienkurse des Forschungszentrums (Jülich KFA)* ch 24
[35] Bansmann J, Lu L, Getzlaff M and Meiwes-Broer K H 1997 *Z. Phys.* D **40** 570
Lu L, Bansmann J and Meiwes-Broer K H 1998 *J. Phys.: Condens. Matter* **10** 2873
[36] Weber W, Back C H, Bischof A, Pescia D and Allenspach R 1995 *Nature* **374** 788
[37] Berger A, Linke U and Oepen H P 1992 *Phys. Rev. Lett.* **68** 839
[38] Chuang D S, Ballentine C A and O'Handley R C 1994 *Phys. Rev.* B **49** 15084
[39] Krams P, Hillebrands B, Güntherodt G and Oepen H P 1994 *Phys. Rev.* B **49** 3633
[40] Kawakami R K, Bowen M O, Choi H J, Escorcia-Arparicio E J and Qiu Z Q 1998 *Phys. Rev.* B **58** R5924
[41] Wulfhekel W, Knappmann S and Oepen H P 1996 *J. Appl. Phys.* **79** 988
[42] Chen J and Erskine J L 1992 *Phys. Rev. Lett.* **68** 1212

[43] Heinrich B, Cochran J F, Kowalewski M, Kirschner J, Celinski Z, Arrot A S and Myrtle K 1991 *Phys. Rev.* B **44** 9348
Krams P, Lauks F, Stamps R L, Hillebrands B and Güntherodt G 1992 *Phys. Rev. Lett.* **69** 3674
[44] Boukari S, Balay J, Beaurepaire E, Biechel G, Carrière B, Deville J P, Muller B and Scheurer F 1999 *Vacuum* **52** 327
[45] Van Dijken S, Di Santo G and Poelsema B 2001 *Phys. Rev.* B **63** 104431
[46] Oepen H P, Millev Y T, Ding H F, Pütter S and Kirschner J 2000 *Phys. Rev.* B **61** 9506
[47] Chaumin Midoir A, Magnan H, Barbier L, Le Fèvre P and Chandesris D 2002 *Appl. Surf Sci.* **188** 115
[48] Giesen M, Schmitz F and Ibach H 1995 *Surf. Sci.* **336** 269
[49] Clarke A, Jennings G, Willis R F, Rous P J and Pendry J B 1987 *Surf. Sci.* **187** 327
Schmidt A K and Kirschner J 1992 *Ultramicroscopy* **42–44** 483
[50] Fassbender J, Allenspach R and Durig U 1997 *Surf Sci.* **383** L742
Nouvertné F, May U, Bamming M, Rampe A, Korte U, Guntherodt G, Pentcheva R and Scheffler M 1999 *Phys. Rev.* B **60** 14382
[51] Newville M, Ravel B, Haskel D, Rehr J J, Stern E A and Yacoby Y 1995 *Physica* B **208/209** 154
[52] Schneider C M, Bressler P, Schuster P, Kirschner J, de Miguel J J and Miranda R 1990 *Phys. Rev. Lett.* **64** 1059
[53] Néel L 1954 *J. Phys. Radiat.* **15** 376
[54] Arias R and Mills D L 1999 *Phys. Rev.* B **59** 11871
Bruno P 1988 *J. Appl. Phys.* **64** 3153